Aerodynamic Optimization of Unmanned Aerial Vehicle through Propeller Improvements

A. F. ElGhazali and S. S. Dol[†]

Mechanical Engineering Department, Abu Dhabi University, Abu Dhabi, Abu Dhabi, UAE

†*Corresponding Author Email: sharulshambin.dol@adu.ac.ae*

ABSTRACT

This paper aimed at presenting a number of suggested improvements that can enhance the performance of a multi-rotor Unmanned Aerial Vehicle. Evaluating each suggestion in terms of the added benefits and feasibility concluded a final choice, which is incorporating a sinusoidal leading-edge profile to the propeller. This choice was numerically investigated with ANSYS Fluent 16.1 through the SST K-Omega turbulence model. The performance of the modified propeller was assessed by comparing the lift and drag results to the same propeller with a straight leading-edge under the same conditions. Both models were studied at pre-stall and post-stall conditions to see the performance effect with respect to the angle of attack. The findings of this research showed 7% increase in the lift force and coefficient that were associated with the addition of the sinusoidal leading-edge including improved recovery from stall spanning from angle of attack that extends between 10° to 25°. This research also provides more insights into how the delayed stall and improved lift help the multirotor to extend flight time and carry heavier payloads. It allows for the exploration of the inner working of the sinusoidal leading-edge and its relationship with the flow field over the propeller.

Keywords: Unmanned aerial vehicle; Numerical investigation; Stall; Sinusoidal leading-edge.

NOMENCLATURE

b	span	Re	Reynold's number
c	chord	S	propeller projected area
C_d	drag coefficient	V	fluid velocity
C_{Di}	coefficient of induced drag		
C_l	lift coefficient	α	angle of attack
D	aerodynamic drag force	ρ	fluid density
L	aerodynamic lift force	υ	kinematic viscosity
Q	volumetric flow rate	ω	rotational velocity of the propeller

1. INTRODUCTION

Unmanned Aerial Vehicle (UAV) is a remotely operated aircraft that functions without the need of an onboard pilot. It operates autonomously or through a remote pilot control (Gupta *et al.* 2013) UAVs are categorised based on aerodynamics into Fixed-wing aircraft, chopper, multi-copter, and motor parachute and glider. This paper focuses on the multi-copter model, which is used for surveillance purposes and monitoring, due to its ability of vertical take-off, landing and hovering compared to fixed-wing aircrafts. The problem with multirotor is the high-power consumption that directly constitutes to its limited endurance. Equations (1) and (2) demonstrate the affecting factors in calculating power consumption in Watts and thrust generation in Ounces (Singhal *et al.* 2018). As can be seen, the pitch "P" (the distance moved forward with a single revolution from the propeller), the propeller diameter "D" and motor rotational velocity "RPM" are important in determining the performance of the multi-rotor. An example of this is that a propeller with a 4.8-inch pitch and 14-inch diameter rotating at 11,000 RPM generates close to 160 Oz of thrust demanding 1308 W of power.

$$Power = P \times D^4 \times RPM^3 \times (5.33X10^{-15}) \quad (1)$$

$$Thrust = P \times D^3 \times RPM^2 \times (10^{-10}) \quad (2)$$

Current commercial UAVs are available in the global market ranging from 5 to 28 minutes in flight time with approximate weight from 0.32 to 4.9 kg

(Colomina and Molina, 2014)Flight time and maximum carrying load vary with each application which decides the coverage area, maximum altitude, climb rate, and stability, but it is always preferable to have plenty of both (Torun, 2000)Thus, to reduce weight, light materials are used consisting of Aluminium, Titanium, and Alloys for metallic materials; whereas, for non-metallic materials transparent and reinforced plastic is used (Soutis, 2005). On the other hand, to improve thrust and increase maximum payload, aerodynamic design of propellers and airframe must be considered. The propellers are an essential component of the design that has the most direct effect on performance making it an interesting component to choose for enhancement.

This paper accordingly focuses on areas of improvement for propeller design that can increase the performance of a multirotor UAV. This will be met through the investigation of some geometric modifications to meet a better aerodynamic performance, those include the implementation of ducting, increasing the aspect ratio, and integration of leading-edge bumps. The models investigated in this research aim at numerically studying and assessing their impact on fluid flow and performance. All these geometric improvements are assessed individually leading to a final choice that is the most effective and feasible from a manufacturing standpoint. An initial assessment is done to the working environment to assure the validity of the design and to determine the boundary conditions.

2. DUCTING

The principle of ducting with rotary airfoil is promising in terms of increased lift and reduced drag forces which yield a longer flight time depending on the application. The use of this technique is not quite popular by UAV manufacturers. There are different aspects that must be investigated to decide whether to use ducting in UAV or not. These are discussed in the coming sections.

2.1 Contribution to the Lift/Drag Forces

Ducting eliminates most of the pressure-induced drag while an efficient design can generate as much as double the lift; this is subject to Reynold's number of the free stream. In the case of high forward velocities, the losses are significantly reduced while some lifts can be generated. If the duct was designed to have an annular wing setup, it can harness the Bernoulli's effect and work as an airfoil. Bernoulli's effect demonstrates the relationship between the speed of a flowing fluid and its pressure. It states that an increase in the flow speed is accompanied by a decrease in pressure while a decrease in speed increases pressure.

Figure 1 demonstrates how a statically operating ducted propeller can contribute to generating additional thrust. The additional thrust is generated when the high-velocity air flows above the inner surface of the duct creating a low-pressure zone (Region 1). This zone has a lower pressure value relative to the air under the inlet (Region 2) creating

a pressure difference. This occurs if the inlet area is larger than the outlet area creating a bell-mouth duct, and the total thrust will equal the net pressure on duct added to the net pressure on the rotor (Leidi *et al.* 2004).

This setup is optimal for static operation (hovering). However, at high forward velocities when the multi-rotor is moving vertically, this setup does not contribute with significant improvement due to the added drag of the body. With the design of UAV, it is important to realise that most of the operating conditions are when the UAV is moving, making it ineffective from an aerodynamic point of view to install ducts to the propellers.
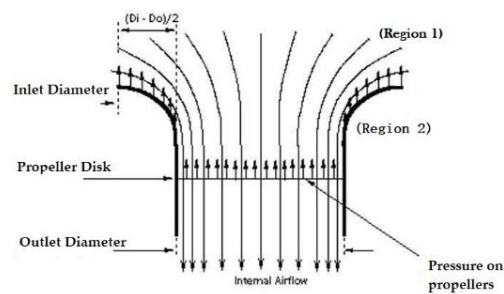
Fig. 1. Schematic presentation of ducted propeller operating statically (zero free stream velocity) (Leidi *et al.* 2004)
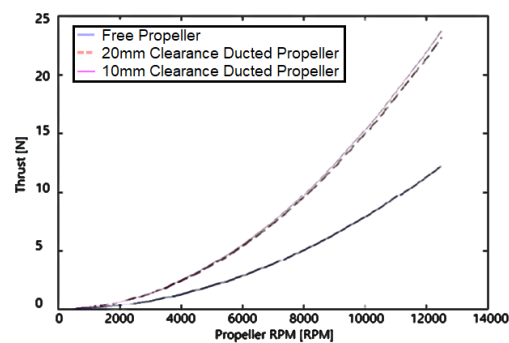
Fig. 2. Thrust versus propeller RPM (Nagpurwala, PEMP RMD 2501).

Figure 2 shows the relationship between the propeller speed and the thrust generated. The graph states that the increase in thrust done by the ducting is proportional to the propeller rotational velocity.

2.2 Limited Air Intake and Exhaust

Another limitation that ducting imposes is the restriction of air flow. This is done due to the physical barrier that the duct walls create around the propeller. Thus, limiting the air intake and exhaust by reducing the volumetric flow rate. This will reduce the amount of thrust that is generated rather than increase it.

2.3 Manufacturing

The manufacturing part is rather challenging with this setup due to the level of accuracy that needs to be maintained. In most ducted propellers, the
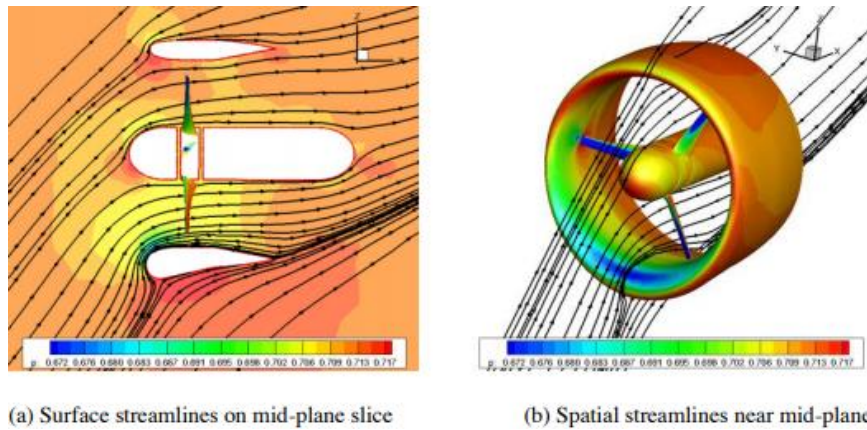
(a) Surface streamlines on mid-plane slice   (b) Spatial streamlines near mid-plane

Fig. 3. Demonstration of the self-stabilization mechanism in ducted propellers (Xu *et al*. 2015).

clearance between the blade tips and the duct is in terms of millimetres or less to assure the minimum pressure loss.

2.4 Stall

In the case of UAV, it is important to be able to move in the same plane maintaining the same altitude. This is achieved by increasing RPM of one of the opposite propellers to create a horizontal force component driving the UAV. But with the implementation of ducts, aerodynamics interference can prevent the UAV from moving creating a stall. The stall is created by the unbalanced pressure distribution on the duct lips creating a self-stabilizing mechanism that prevents the UAV from moving horizontally at high speeds. This is further explained by a numerical study made by Xu *et al.* (2015) in the National Key Laboratory of Science and Technology on Aerodynamic Design and Research, Xi'an, China.

Following on from the discussion above, it can be inferred that ducted propellers are not widely used by UAV manufacturers to enhance aerodynamic abilities. However, they are often used as a safety precaution, but the weight penalty must be taken into consideration while designing.

3. ASPECT RATIO

According to Wood (2019), "aspect ratio is the ratio of the span of the wing to its mean chord". The equation in Fig. 4 demonstrates this ratio and how it can be calculated. This parameter is vital when improving the design of a wing profile because the increase of the aspect ratio means that the wing will be longer and thinner compared to original design if the weighted area for both was equivalent. The improvement that this change makes is correlated to the pressure drag and downwash effect. When the wing tip has less region for the transfer of pressure between the top and the bottom creating downwash, the flow rate of air will be lower thus less overall pressure losses.

$$c_d = \frac{D_f + D_p}{q_\infty S} \tag{3}$$

$$C_{D,i} = \frac{D_i}{q_\infty S} \tag{4}$$

Equations (3) and (4) define the two contributing components of the overall coefficient of drag c_d, friction drag donated by D_f and pressure drag D_p. For a finite wing, an additional source of induced drag emerges D_i and can be reduced by improving the aspect ratio of the wing.
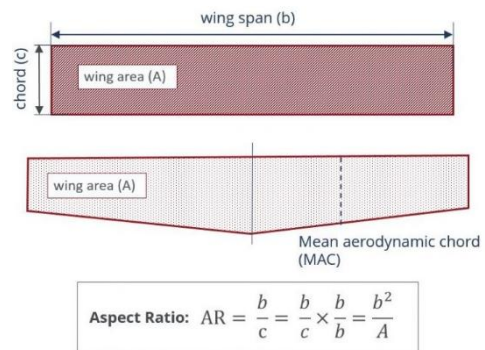

Fig. 4. Definition of Aircraft Aspect Ratio (Wood, 2019).

Table 1 is a proposed increase in the Aspect Ratio of a reference UAV propeller design

parameters	RB-Tmo-101	Improved Design
Span length	143 mm	175 mm
Mean Chord	33 mm	27 mm
Aspect Ratio	4.33	6.48
Weighted area	$47.19\ cm^2$	$47.25\ cm^2$

Fig. 5. A scalable measure of the increased AR (T-Motor, 2019).
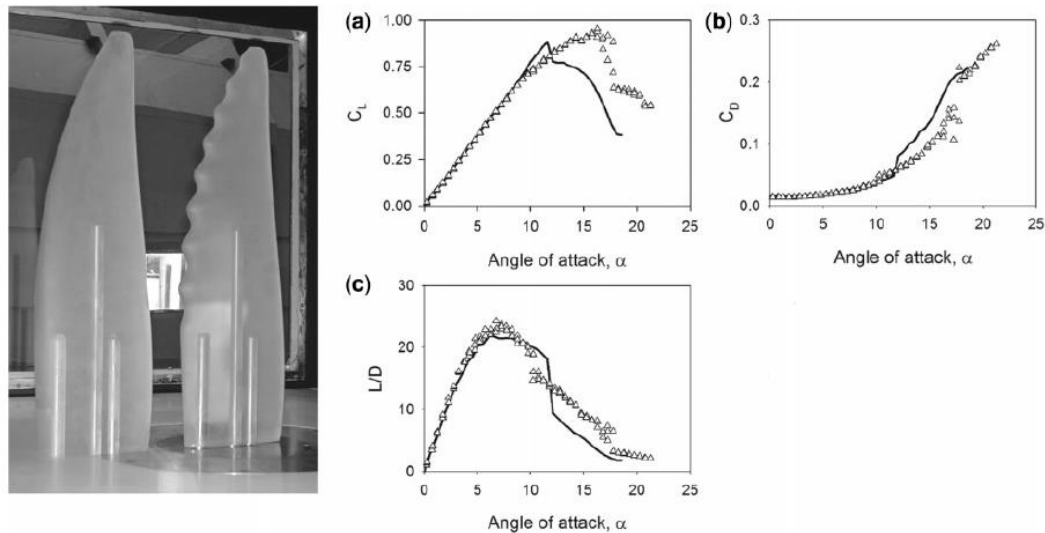
Fig. 6. Effect of tubercles on the coefficient of lift, drag, and Aerodynamic efficiency (Fish *et al*. 2008).

Fig. 7. Photo of tubercles on the humpback whale fin (AskNature, 2016).

From the geometry modification, the increase in aspect ratio was accompanied by a slight increase in the weighted area. However, the limitation in the new design is the clearance gap between each propeller in the multi-rotor. For a test model quadcopter, the clearance gap was 11 cm estimated and with the increased aspect ratio, it became 5 cm thus limiting the design.

4. LEADING-EDGE BUMPS

4.1 Rotating Stall

A limiting factor of performance in UAVs is rotating stall. Rotating stall is generated when separation occurs between the blades and the incoming flow due to instabilities in the flow direction, which usually happens when the wind is strong and chaotic. These instabilities may arise when the upstream flow direction with respect to the fixed pitch (angle of attack of the propellers) change, exceeding the stall angle of attack. This stall is problematic as it occurs in a form of shock generating high levels of vibrations and noise with efficiency and lift loss.

4.2 Inspiration from Biomimetics and Nature

Inspiration from nature can help solve certain problems, through years of evolution to adapt, survive, and develop. Animals provided exceptional solutions in many areas including aerodynamics and hydrodynamics. These solutions are not always feasible due to its high level of complexity making it in some cases nearly impossible to replicate, for instance, the designing of a mechanical bat. Nevertheless, we gain a lot of insight into how these biomechanical systems operate and learn from them. Also noting that most of these phenomena are in a very low range of Reynolds number which makes them impractical for most turbomachinery and aerodynamic applications.

Marine biologists came across the distinctive shape of the humpback whale flippers that allow them to do sharp rolls and loops beneath the water surface. These flippers are characterised by the number of features including rounded tubercles on its leading-edge (10 to 11), starting off about 30% from the flipper root with constant inter-tubercle distance, and the chord reduces moving outward (Fish and Battle, 1995). All these features affect the flow field characteristics positively keeping the boundary layer attached to the fin maintaining lift at higher angles of attack and operate as a stall control system. This helps in flattening the lift curve in the post-stall region thus helping in moving under near-stall conditions due to the unsteady flow field.

4.3 Mechanism

In simple words, the wavy leading-edge made by the tubercles generates streamwise vortices that change the coefficient of lift and drag values with different angles of attack. Johari *et al.* (2007) conducted an experimental investigation on a two-dimensional airfoil with modified sinusoidal leading-edge following these presuppositions: Wing type: NACA 63_4-021, Reynolds number: 183,000 angle of attack range: $6 \leq \alpha \leq 30$ degrees, Amplitudes range of sinusoid: 2.5% to 12% of the chord. The data were collected from two regions; the first was for angles of attack lower than the critical; whereas the second was for higher than the critical α. For the first set, the results were not promising as a decrease in lift and increase in drag was observed. But, on the second set, the results continuously confirmed an increase in lift reaching 50% and almost no increase in drag. One of the important insights was that the results showed independence with respect to the wavelength making it not regarded as an important parameter. On the other hand, the main variable that affected the performance was the amplitude of the sinusoid.

Suggesting that from all the previous choices the implementation of leading-edge bumps is the most promising as it will help with adding two advantages. First, work as a stall delay mechanism preventing UAVs from sudden drops in altitude when not enough lift is generated. Thus, saving the UAV from crashing and losing valuable equipment. Second, the flattening of the lift curve after the critical α will be of a major advantage because it will allow manufacturers to safely use large pitch propellers making the propeller capable of producing more thrust with the same energy demand from the batteries, thus less power consumption and positively increasing the flight time. Simultaneously, the ability to increase the propeller pitch without sacrificing power can come in handy if the multi-copter is optimised for carrying heavy payloads. Therefore, the objective of the propeller with integrated leading-edge bumps studied in this paper is to provide the UAV manufacturer with the freedom to choose between a model with larger thrust levels for the same power consumption or improved flight time.

5. NUMERICAL ASSESSMENT

In this section, a numerical analysis is done for the propeller with the added sinusoidal leading-edge to test the level of improvement that provides with an insight into the characteristics of the changed flow field. The CAD software used for the designing is ANSYS Workbench and the solution and post-processing is done using the CFD simulation software ANSYS Fluent 16.1. In order to see the effect created by the leading-edge bumps, several models are analysed. These models are divided into two sets: the first set consists of blades with a straight leading-edge; whereas the second set consists of blades with sinusoidal leading-edge. All models have the same cross-section of NACA 6409 airfoil, span, chord, and dimensions. The sinusoidal leading-edge blades with their straight leading-edge counters

taken as reference models are studied separately at ten values of angles of attack. This covers a wide range of angles giving a comprehensive look at the performance of the modified blade. Yielding a total of 20 models to be analysed at 10 angles of attack. The values of α are chosen to examine the flow characteristics of the lift/drag curves at pre-stall, stall, and post stall regions.

Table 2 Tested models

Angles of attack	Straight leading-edge blade	Sinusoidal leading-edge blade
$\alpha = 0^o$	Pre-Stall	Pre-Stall
$\alpha = 3^o$	Pre-Stall	Pre-Stall
$\alpha = 5^o$	Pre-Stall	Pre-Stall
$\alpha = 8^o$	Pre-Stall	Pre-Stall
$\alpha = 10^o$	Stall	Stall
$\alpha = 13^o$	Post-Stall	Post-Stall
$\alpha = 15^o$	Post-Stall	Post-Stall
$\alpha = 17^o$	Post-Stall	Post-Stall
$\alpha = 21^o$	Post-Stall	Post-Stall
$\alpha = 26^o$	Post-Stall	Post-Stall

5.1 Numerical Model

The model chosen for this study is SST K-Omega (SST k-ω) in ANSYS Fluent, which provides accurate results for flow separation and turbulence simulation especially when analysing post-stall conditions.

SST k-omega Governing Equations (Menter, 1994)

Turbulence Kinetic Energy

$$\frac{\partial k}{\partial t} + U_j \frac{\partial k}{\partial x_j} = P_k - \beta^* k\omega + \frac{\partial}{\partial x_j}\left[(\nu + \sigma_k \nu_T)\frac{\partial k}{\partial x_j}\right] \quad (5)$$

Kinematic Eddy Viscosity

$$\nu_T = \frac{a_1 k}{\max(a_1\omega, SF_2)} \quad (6)$$
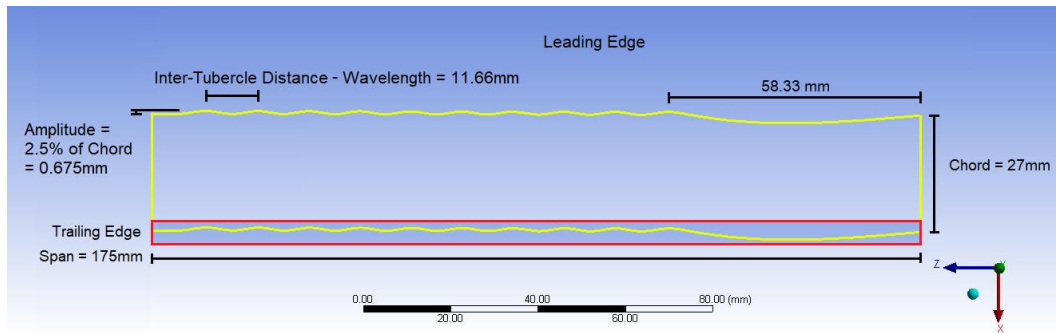
5.2 Boundary Conditions

Propellers are rotating machinery governed by the equations that describe this form of motion similar to polar moment of inertia and centrifugal force which are used for calculations. Another aspect is the place of application, in this case fluctuating wind speeds and directions meaning that the flow is turbulent with a medium of air with standard properties at sea level. After knowing these values, Reynolds number is calculated as an average of the wingspan. To determine the rotational velocity of the wing, the electric motor RPM is used through the following.

$$\omega = v/2\pi b \quad (7)$$

$$V = 2\pi b\omega$$

$$V = 2\pi * 0.175\, m * \frac{5500\, rpm}{60s} = 100.793\, \frac{m}{s} \quad (8)$$

This is the tangential velocity of the wing tip at its maximum diameter. To get the average velocity of the entire wing, the velocity profile is formulated as an integral equation and then solved.

Fig. 8. Schematic of the wing incorporating bumps.

$$V_{avg} = \frac{1}{b-0} \int_0^b V(b) \, db \qquad (9)$$

$$V(b) = 575.96b \qquad (10)$$

$$V_{avg} = \frac{1}{0.175-0} \int_0^{0.175} 575.96b \, db = 50.396 \frac{m}{s} \qquad (11)$$

The next step is to calculate Reynold's number.

$$Re = \frac{Vc}{\upsilon} = \frac{50.396\frac{m}{s}*0.027m}{1.562 \times 10^{-5} \, m^2/s} = 87113.03 \qquad (12)$$

Table 3 Boundary conditions

| property	value
Kinematic viscosity	$1.562 \times 10^{-5} \ m^2/s$
density	$1.184 \ kg/m^3$
temperature	$25 \ C^\circ$
pressure	$1 \ atm$
chord	27 mm
span	175 mm
Projected area	$0..00472637 \ m^2$
V_{max}	$100.793 \ m/s$
V_{avg}	$50.396 \ m/s$
Re	87113.03
Motor speed	$5,500 \ rpm$

5.3 Pre-Processing

The geometry of the bumped leading-edge propeller follows the design specifications of the humpback whale flippers. This includes 10 bumps attached to the leading-edge each of them has an amplitude of 2.5% of the chord and starts from a distance equals third of the span from the blade root. The distance separating the bumps is constant and the trailing-edge also incorporates bumps to see if any effect would occur on the flow leaving the wing. Figure 8 exemplifies the dimensions of the bumps shape and Fig. 9 is a top view comparison between the profile of the bumped and straight leading-edge models.

The computational domain is composed of over 2.4×10^6 tetrahedral cells creating a sufficiently dense mesh to assure accuracy and grid convergence. In addition, the rectangular enclosure has an inlet face, an outlet face, and four walls with enough spacing to eliminate the boundary layer at the walls from interacting with the model. The computational domain is enlarged to have 80 mm separating the

model from all enclosure boundaries with expansion of the trailing-edge downstream region to give a better extent for the wake as illustrated in Fig. 11.
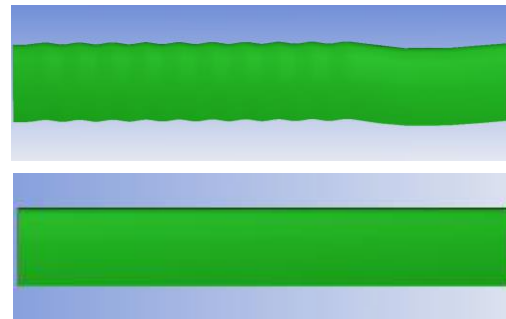
**Fig. 9. Profile of the bumped leading-edge (lift) and straight leading-edge (right).**
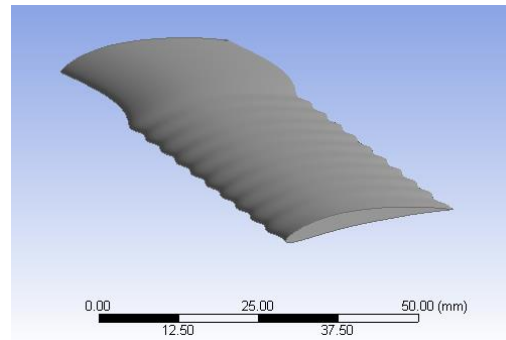
Fig. 10. Bumped leading-edge wing geometry.

5.4 Grid Independence Study

Meshing is done manually to assure grid independent analysis. This is done by refining the leading-edge and other critical surfaces for all models. To determine the number of cells and the element size required to reach independence, the element size is reduced repeatedly until a satisfying mesh density is reached.

The process of choosing the correct element size started by a big element size of 40 mm. The mesh was coarse thus the size was reduced to 30 mm then to 20 mm. However, large difference percentages are still observed. Further reduction was done as in table 4 until reaching a 0.1 mm element size which has the

lowest percentage difference for both coefficients. The refined mesh and large number of elements used successfully achieved convergence for all 20 models.
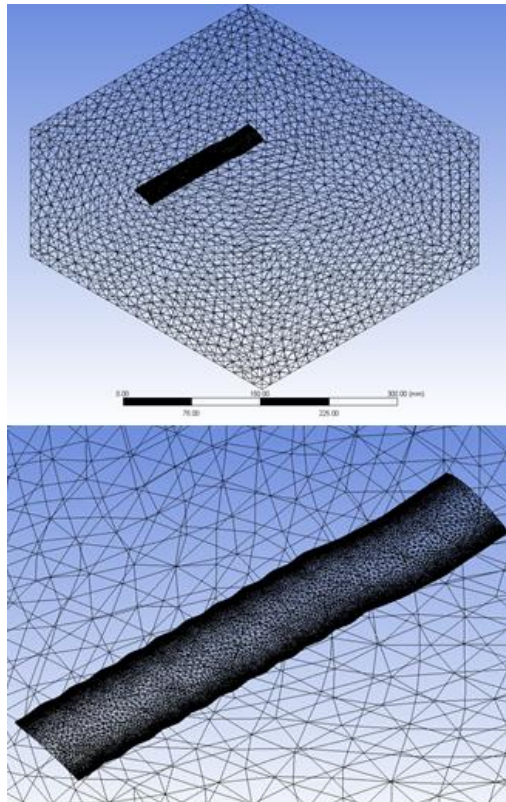
Fig. 11. Computational domain (top) and mesh over the model (bottom).

Table 4 Grid independence study

Element size	Cells No.	c_l deflection %	c_d deflection %
10 mm	100,028	-	-
5 mm	297,806	0.9 %	4 %
1 mm	480,398	0.2 %	2 %
0.2 mm	2,223,344	0.05 %	1.1 %
0.1 mm	2,477,202	0.04 %	0.9 %

6   RESULTS AND DISCUSSION

The results obtained from the numerical solver are shown in table 5. Each model has the net lift and drag forces and their coefficients presented. Additionally, the drag force is divided into two components: the pressure and shear drag to see which contributes the most. In order to draw conclusions from the numbers, a percentage difference column is added describing the difference in values between the bumped leading-edge wing compared to the straight leading-edge model. Figure 12 and 13 demonstrate lift coefficient and drag coefficient verses the angle of attack respectively. It is worth noting that stall occurs at $\alpha = 10^o$ separating the graphs into pre-stall and post-stall regions each having distinctive features.

The data analysis shows a clear change in the aerodynamic characteristics for the modified models. Notably, different lift and drag values are noticed indicating a change in the flow field around the wings. Starting with the models studied before stall occurrence (angles lower than $\alpha = 10^o$ for NACA 6409), the change in lift/drag values is relatively small with a slight decrease in lift a maximum of 4.56% with negligible drag deflection. Lift force and coefficient showed a decrease of 5.4 % compared to the straight leading-edge model showing the extent of effect that the geometry modification has. For the post-stall models, the percentage change in aerodynamic values is significantly larger than at pre-stall, reaching a maximum of 12.73% change. The lift force benefits from the bumps experiencing a positive increase reaching 12.67 N with a higher coefficient of lift at $\alpha = 21^o$ and across most other angles. However, a noticeable increase in drag force is present reaching 1.75 N mostly originating as pressure drag at the same angle. This increased the drag coefficient of the straight leading-edge wing by a magnitude of 10.54% whilst adding the bumps noting that for other angles drag is minimally influenced. This implies that at post-stall, both lift and drag forces have major evolution.

The data analysis also shows consistency with previous studies like the findings of Corsini, *et al.* (2013). Their study was conducted on symmetric (NACA0015) and compared (NACA4415) airfoils with both bumped and straight profiles. The added bumps provided a lift increase for both airfoils in post-stall most notably for the symmetric achieving stall recovery by 40% improved lift at $\alpha = 24^o$, with a slight addition of drag to the symmetric airfoil and none for the chambered. The chambered airfoil (NACA4415) stalled at $\alpha = 23^o$ making $\alpha = 20^o$ in the pre-stall region while it is considered at post-stall in this study indicating different airfoils react dissimilarly by adding bumps, obtaining different performance levels under the same conditions. Emphasising the importance of the airfoil chosen for the study putting it among the most important parameters when studying propeller performance.

The study also emphasised that the increase in the amplitude of the sinusoid flattens the lift curve and affects the performance. It was also found that the stall delay is insensitive to the wavelength of the bump's distribution on the sinusoid.

6.1   Effects of the Leading-Edge Bumps

To see the reason for getting the transformed lift/drag values, the velocity and pressure fields are analysed. Fig. 14 is a frontal view of the leading-edge showing pressure coefficient variations for the standard and modified wing in post-stall operation. At the top contour pockets of minimum pressure are the sinusoid troughs dislocated by the peaks spreading along the span. The modified profile exhibits a larger pressure coefficient difference between the two sides of the wing compared to the standard, and hence improved lift without separation.
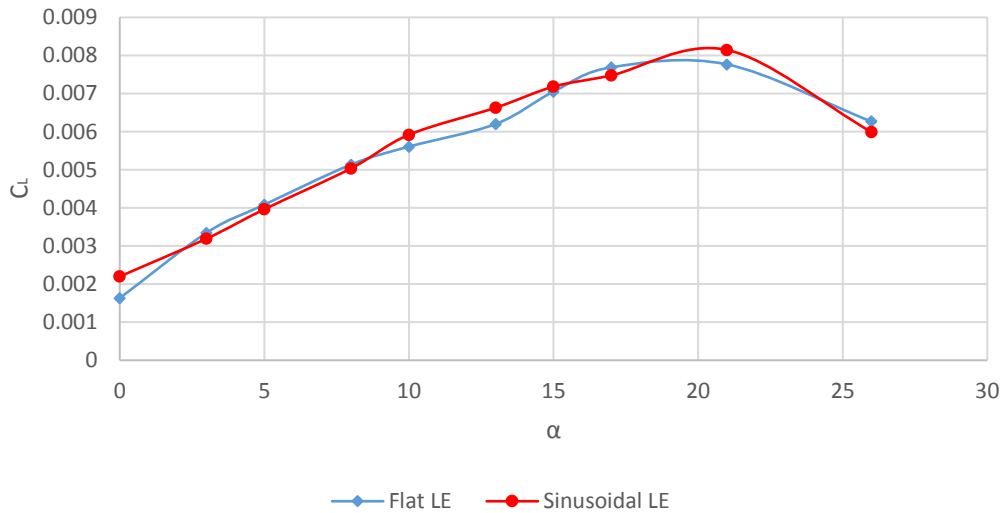
Fig. 12. Lift coefficient against angle of attack for sinusoidal leading-edge and reference blades.
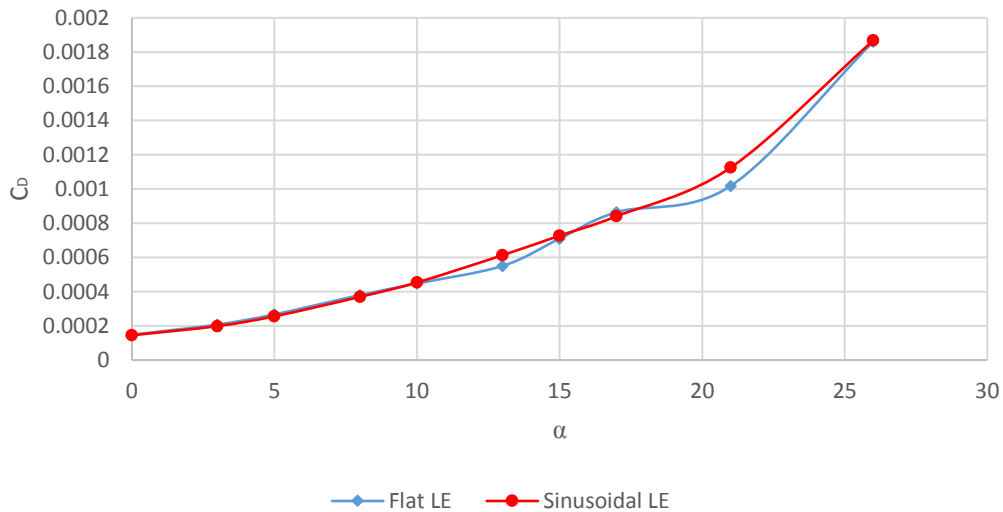

Fig. 13. Drag coefficient against angle of attack for sinusoidal leading-edge and reference blades.
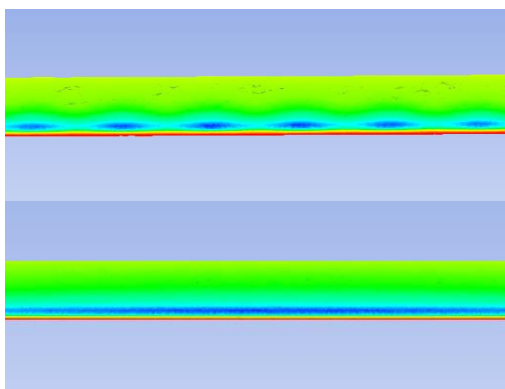

Fig. 14. Pressure distribution on the leading-edge for the sinusoidal profile (top) and flat profile (bottom) at $\alpha = 13^o$.

Additionally, Fig. 16 demonstrates the streamlines distribution with a visible increase in circulation for the bumped profile on the suction side. The vortex generated and the local velocity of the flow are considerably larger with comparison to the straight profile which is showing separation at $\alpha = 26^o$. The increase in velocity component can be better understood from Fig. 15 which shows the velocity vectors distribution on the wing cross-section. This distribution is a function of the spanwise position and more importantly whether the contour is at a peak, a trough, or in between because each has a different flow characteristic. In part (b) which is taken at a trough, the orientation of the generated vortex helps with accelerating the incoming flow to reach high velocities.

An explanation for this phenomenon and the reason for the generation of vortices is the mechanism that creates circulation at the leading-edge. At the first contact point between the incoming flow and the wing, the peak of the sinusoid experiences a stagnation point. This point has high pressure
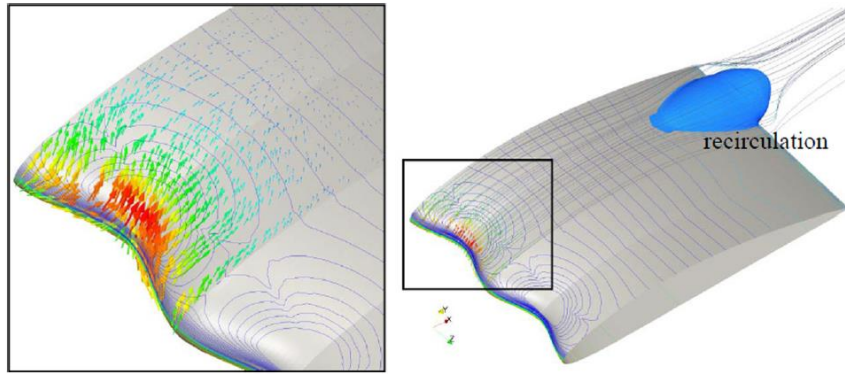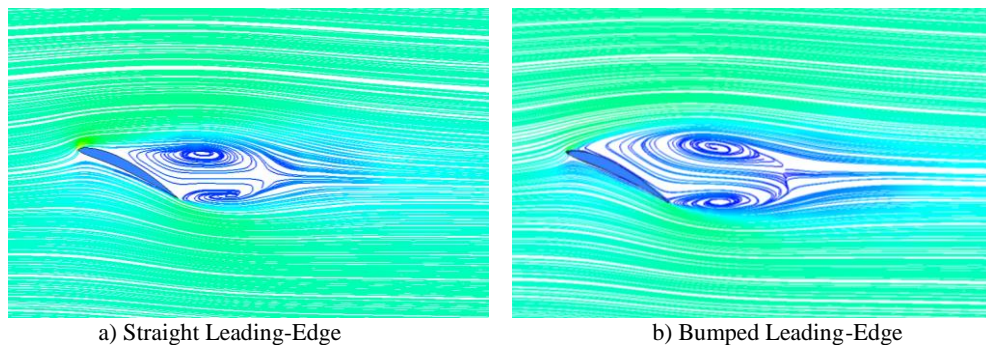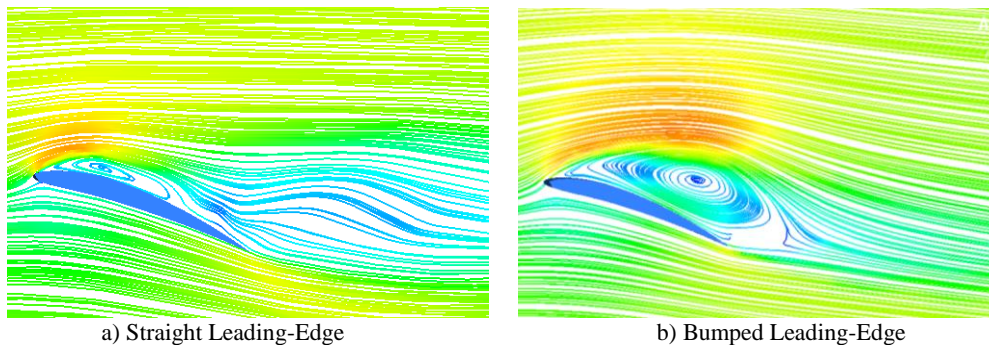
Fig. 15. Insight on the distortion of the velocity field generated by the leading-edge (2D vectors constructed with span and pitch-wise velocity components) (Corsini *et al.* 2013).

a) Straight Leading-Edge   b) Bumped Leading-Edge
Fig. 16. A sectional view of streamlines on both models at α = 26°.

a) Straight Leading-Edge   b) Bumped Leading-Edge
Fig. 17. A sectional view of streamlines for both models with double the velocity magnitude at Re = 174, 226 and α = 20° under the same conditions.

redirecting the flow into the trough and accelerating it in the process. This makes the incoming air reach a higher velocity at the trough reducing pressure compared to the peak. The difference in pressure between each consecutive trough and peak accompanied with regions of fast and slow flowing air creates velocity gradients that initiate circulation at the suction side of the wing. The generated streamwise vortices are useful in the sense that they reenergise the flow and increase the momentum transfer by helping it in keeping the flow attached to the wing surface and delaying stall as Fig. 14 illustrates.

6.2   Application on Multi-Rotor

The main advantage that a multi-rotor gains by incorporating the modified propellers is the performance leap. The more capable propellers can be used in different manners to be most beneficial for the designer depending on the purpose of use.

Generally, the UAV can follow two tracks: the first is to make use of the added thrust by carrying heavier payloads if transportation is the main target. To put this in perspective, the wing studied is 175 x 27 mm capable of generating 46.5 N which equals 4.7 kgs of thrust at 11,000 RPM with the expense of extra drag. This is only half the propeller, thus for a quadcopter, two wings for each propeller with four propellers total yields a maximum of 37.9 kgs of thrust from a relatively a small sized system. The case study done by Rajendran *et al.* (2016)

Table 5 Results of analysis

	Lift force (N)	Lift coefficient C_l	Drag force (N)	Pressure drag force (N)	Viscous drag force (N)	Drag coefficient C_d
Flat LE at α=0°	2.5365	1.63E-03	0.2299	0.1228	0.1070	1.48E-04
Sinusoidal LE at α=0°	3.4216	2.20E-03	0.2249	0.1214	0.1035	1.45E-04
% change	+34.89%	+34.90%	-2.17%	-1.14%	-3.27%	-2.17%
Flat LE at α=3°	5.2039	3.35E-03	0.3231	0.2189	0.1041	2.08E-04
Sinusoidal LE at α=3°	4.9667	3.19E-03	0.3087	0.2042	0.1045	1.98E-04
% change	-4.56%	-4.56%	-4.46%	-6.72%	+0.38%	-4.49%
Flat LE at α=5°	6.3518	4.08E-03	0.4149	0.3098	0.1050	2.67E-04
Sinusoidal LE at α=5°	6.1671	3.96E-03	0.3978	0.2931	0.1046	2.56E-04
% change	-2.91%	-2.91%	-4.12%	-5.39%	-0.38%	-4.12%
Flat LE at α=8°	7.9910	5.14E-03	0.5907	0.4859	0.1047	3.80E-04
Sinusoidal LE at α=8°	7.8360	5.04E-03	0.5744	0.4697	0.1046	3.69E-04
% change	-1.94%	-1.94%	-2.76%	-3.33%	-0.09%	-2.75%
Flat LE at α=10°	8.7228	5.61E-03	0.6961	0.5918	0.1042	4.48E-04
Sinusoidal LE at α=10°	9.2070	5.92E-03	0.7054	0.5997	0.1055	4.54E-04
% change	+5.55%	+5.55%	+1.34%	+1.33%	+1.25%	+1.35%
Flat LE at α=13°	9.6479	6.20E-03	0.8556	0.7554	0.1002	5.50E-04
Sinusoidal LE at α=13°	10.3139	6.63E-03	0.9533	0.8516	0.1016	6.13E-04
% change	+6.90%	+6.90%	+11.42%	+12.73%	+1.39%	+11.42%
Flat LE at α=15°	10.9702	7.05E-03	1.1033	1.0035	0.0997	7.09E-04
Sinusoidal LE at α=15°	11.1727	7.18E-03	1.1310	1.0314	0.0996	7.27E-04
% change	+1.85%	+1.84%	+2.51%	+2.78%	-0.10%	+2.52%
Flat LE at α=17°	11.9625	7.69E-03	1.3444	1.2477	0.0966	8.64E-04
Sinusoidal LE at α=17°	11.6332	7.48E-03	1.3072	1.2114	0.0957	8.40E-04
% change	-2.75%	-2.75%	-2.77%	-2.90%	-0.93%	-2.76%
Flat LE at α=21°	12.0810	7.77E-03	1.5829	1.4949	0.0880	1.02E-03
Sinusoidal LE at α=21°	12.6722	8.15E-03	1.7498	1.6596	0.0901	1.12E-03
% change	+4.89%	+4.89%	+10.54%	+11.02%	+2.39%	+10.53%
Flat LE at α=26°	9.7442	6.26E-03	2.8947	2.8300	0.0646	1.86E-03
Sinusoidal LE at α=26°	9.3173	5.99E-03	2.9054	2.8458	0.0596	1.87E-03
% change	-4.38%	-4.38%	+0.37%	+0.56%	-7.74%	+0.37%

provides a relation between the propeller size and thrust generated under certain inputs. The thrust level of the modified profile propellers significantly surpasses what most similar sized propellers can provide as indicated in the study. Excluding the UAV weight, this payload capacity expands the possibilities of transport applications.

Moreover, if the payload increase is not a priority, the added trust can be oriented towards extended flight time by reducing the size of the batteries since the extra power is no longer needed. Additional subsidiary benefits of integrating bumps to the propellers are that they provide quieter operation with less vibrations which are helpful for photography purposes. It is important to state that the thrust provided in this study from the modified propeller is a strong function of the airfoil chosen. In

the case of working with another airfoil, the lift/drag values found will be dissimilar. Making the process of choosing the airfoil next to the pitch and size an important task.

7 CONCLUSION

This paper presented several geometry modifications that can improve the performance of a multi-rotor UAV. Each suggestion was discussed and assessed with a final choice of incorporating a sinusoidal leading-edge to the propeller. A numerical investigation was done with ANSYS Fluent 16.1 choosing the SST K-Omega turbulence model for analysis. The performance of the modified geometry was assessed by comparing the lift and drag results to the same propeller with a straight leading-edge. Both geometries are studied at pre-stall and post-stall conditions to see their effect with respect to the angle of attack. An increase in the lift force and coefficient of 7 % was associated with the addition of the sinusoidal leading-edge with improved recovery from stall. The reformed leading-edge profile affected the velocity filed on the propeller by generating circulation and reenergising the flow to remain attached at angles of attack where separation should occur. The delayed stall and improved lift help the multirotor to achieve extended flight time and carry heavier payloads.

REFERENCES

AskNature. (2016, September 14). *Flippers provide lift, reduce drag.* Retrieved from https://asknature.org: https://asknature.org/strategy/flippers-provide-lift-reduce-drag/#.XH_GdCgzbIU

Colomina, I. and P. Molina (2014). Unmanned aerial systems for photogrammetry and remote sensing: A review. *ISPRS Journal of Photogrammetry and Remote Sensing*, 79–97.

Corsini, A., G. Delibra and A. G. Sheard (2013). On the Role of Leading-Edge Bumps in the Control of Stall Onset in Axial Fan Blades. *Journal of Fluids Engineering-transactions of The Asme, 135*(8), 081104.

Fish, F. E. and J. Battle (1995). Hydrodynamic design of the humpback flipper. *Journal of Morphology* 225(1), 51-60.

Fish, F. E., L. E. Howle and M. M. Murray, (2008).

Hydrodynamic flow control in marine mammals. *Integrative and Comparative Biology* 48(6):788-800.

Gupta, S. G., M. M. Ghonge and D. P. Jawandhiya, (2013, April). Review of Unmanned Aircraft System (UAS). *International Journal of Advanced Research in Computer Engineering & Technology (IJARCET)* 2, 1646-1658.

Johari, H., C. W. Henoch, D. Custodio, and A. Levshin, (2007). Effects of Leading-Edge Protuberances on Airfoil Performance. *AIAA Journal* 45(11) 2634-2642.

Leidi, M., N. Rohrseitz, L. Roos, and Y. Luchessa (2004). *a multigravity robot.* Lausanne, Switzerland: Autonomous Systems Laboratory 1, European Space Agency.

Menter, F. R. (1994). Two-Equation Eddy-Viscosity Turbulence Models for Engineering Applications. *AIAA Journal* 32(8),1598-1605.

Nagpurwala, Q. (PEMP RMD 2501). *Ducted Fans and Propellers.* Bangalore: M. S. Ramaiah School of Advanced Studies.

Rajendran, P., H. Smith, K. I. Yahaya, and N. M. Mazlan, (2016, September). Electric Propulsion System Sizing for Small Solar-powered Electric Unmanned Aerial Vehicle. *International Journal of Applied Engineering Research* 11, 9419-9423.

Singhal, G., B. Bansod, L. Mathew (2018, November). Unmanned Aerial Vehicle Classification, Applications and Challenges: A Review. *Preprints*, 2.

Soutis, C. (2005). Fibre reinforced composites in aircraft construction. *Progress in Aerospace Sciences* 42 (1), 143-151.

T-Motor. (2019, March 6). *T-Motor 14" x 4.8" Carbon Fiber Propeller Pair*.

Torun, E. (2000). *UAV Requirements and Design Consideration.* Yucetepe, Ankara/ TURKEY: Technical & Project Management Department, Turkish Land Forces Command.

Wood, A. R. (2019, March 6). *https://aerotoolbox.net/aspect-ratio*. Retrieved from https://aerotoolbox.net: https://aerotoolbox.net/aspect-ratio/

Xu, H. Y., Xing, S. L. and Ye, Z. Y. (2015). Numerical study of ducted-fan lip stall suppression based on. *7th International Conference on Fluid Mechanics, ICFM7* (p. 161). Xi'an: Procedia Engineering 126.